

A study of expansion tube gas flow conditions for scramjet combustor model testing

By F. Örley, C. L. Strand, V. A. Miller, M. Gamba,
N. A. Adams AND G. Iaccarino

1. Motivation and objectives

One of the challenges of ground-based experimental testing of hypersonic flow phenomena are the physical limitations of traditional flow facilities. To generate flows with the high enthalpy and speed characteristic of hypersonic flight, impulse facilities, such as shock tunnel and expansion tube, are typically required. An example is the Stanford Expansion Tube (Heltsley *et al.* 2006) which was designed specifically to replicate scramjet combustor conditions of air-breathing, hypersonic propulsion systems.

The expansion tube, which is the focus of our investigation, is a short-duration facility where the aerothermal conditions of the test gas are generated by an unsteady shock/expansion wave system (Trimpi 1962). Owing to its design and operation, the properties of the test gas in its final state are limited by short test times, flow non-uniformity (spatial and/or temporal), viscous effects (e.g., boundary layer growth; Mirels 1963, 1966*a*; Walker & Dennis 1972), real gas effects and diaphragm rupturing processes (White 1958; Rothkopf & Low 1974; Furukawa *et al.* 2007). Paull & Stalker (1992) give a comprehensive overview of some of the known sources of disturbances and their impact on test gas properties.

Some of our recent work on this facility has focused on the investigation of a fueled scramjet combustor model (Gamba *et al.* 2011). Because this work requires an accurate knowledge of the performance of the facility, the current study aims at investigating the dynamics of the facility, at identifying non-ideal behaviors, and, as the overarching goal, at quantifying temporal and spatial variation of the test gas properties under conditions relevant to the experiments of Gamba *et al.* (2011). Furthermore, this work attempts to build upon other ongoing experimental efforts (Strand & Hanson 2011*b*).

The work reported here is a combined numerical/experimental effort. Axisymmetric, viscous, unsteady RANS simulations of the operation of the expansion tube have been performed. Additionally, measurements of observable quantities have been carried out to validate the simulation and to gain physical insight on the operation into the facility. The work presented here is organized as follows. First, a brief description of the expansion tube process is offered. Then, the unsteady RANS model are presented, followed by a description of the experiments. Finally, the result's section are dedicated to validation of the simulation and investigation of the test gas properties.

2. Introduction to the Stanford expansion tube facility

The Stanford Expansion Tube Facility at the High Temperature Gas Dynamics Laboratory at Stanford University was designed by Heltsley (Heltsley *et al.* 2006). A schematic diagram of the expansion tube is shown in Figure 1. The tube has a total length of 11.95

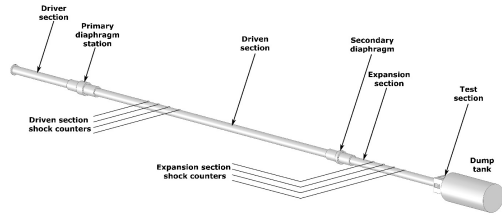


FIGURE 1. Schematic diagram of the Stanford Expansion Tube Facility. Figure adapted from Gamba *et al.* (2011).

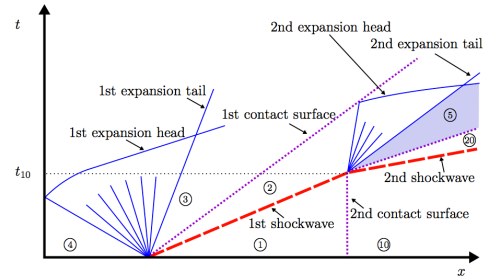


FIGURE 2. Space-time-diagram showing the linearized wave propagation inside an expansion tube facility.

m. It is divided into a 1.9 m long driver, a 7.34 m long driven section and a 2.71 m long expansion section. The tube has an inner diameter of 141 mm.

Trimpi (1962) first offered a theoretical description of the expansion tube as a tool to produce hypersonic flows, as found, for example, in atmospheric re-entry applications. Operation of an expansion tube is based on principles similar to those that describe a shock tube, but features a second unsteady expansion of the test gas that results in total-enthalpy multiplication. The facility consists of a high pressure driver section filled with helium, a low pressure driven section filled with the test gas (e.g., dry air, as in the current study) and a low pressure expansion section filled with helium. All sections are separated by diaphragms. The test section, where test articles are housed, is then located at the outlet of the expansion section.

A schematic diagram of a space-time-plot visualizing the linearized unsteady wave propagation occurring in an expansion tube during a typical test is depicted in Figure 2. Following the rupture of the primary diaphragm, a shock wave propagates into the driven section, instantaneously heating, compressing and accelerating the stagnant test gas from state 1 to state 2. Once the primary shock wave arrives at the expansion section, rupture of the secondary diaphragm induces a second shock wave that propagates into the expansion gas. Simultaneously, a secondary unsteady expansion wave isentropically processes the test gas from state 2 to the desired final state 5. Kinematic conditions at the driven/expansion contact surface impose a uniform pressure and speed across the contact surface. The test time begins with the arrival of the test gas at the outlet of the tube and it ends with the arrival of either the secondary expansion tail, the reflection of the secondary expansion head from the driver/driven contact surface, or the contact surface itself. Typically, the resulting test time is on the order of 0.5 – 1 ms. The short test time is a major limitation of these facilities and makes experimental investigation challenging. In addition, non-ideal effects, such as boundary layers, reduce the test time further and introduce disturbances that limit the uniformity of the test gas (Mirels 1963, 1966*b*; Paull & Stalker 1992).

3. Computational setup

Joe, the second-order order, finite volume unstructured, compressible RANS (Reynolds-averaged Navier-Stokes) solver, was used as the starting point for the unsteady flow computation. The solver includes a flamelet-based chemistry, and was developed in recent years by Pecnik *et al.* (2009) and Terrapon *et al.* (2010), where a detailed description

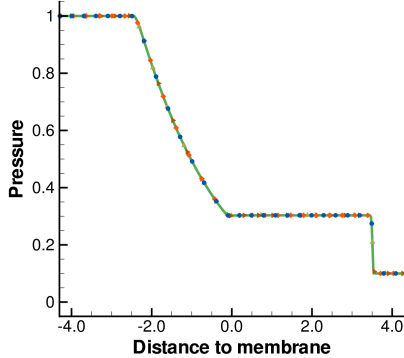


FIGURE 3. Pressure distribution for the shock tube test case of Sod (1978) at a time $t = 2.0$ s for several pseudo-time iteration schemes (explicit, implicit, three- and four-step Runge-Kutta schemes, shown as Delta, Triangle, Diamond and Circle symbols, respectively) and a three-step Runge-Kutta scheme without dual-time-stepping (solid line). Spatial second-order discretization, HLLC approximate Riemann Solver.

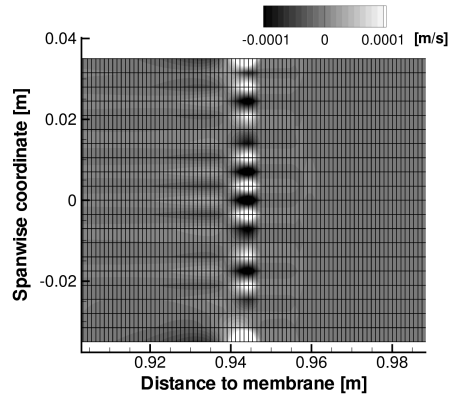


FIGURE 4. Carbuncle phenomenon in a two-dimensional Euler flow: contour plot of the span-wise velocity distribution at the shock front (near $x = 0.94$) on a grid with 20 cells in the span-wise direction and 1,000 cells per meter in the axial direction for a shock Mach number of $Ma \sim 5$.

can be found. The strict object-oriented structure of the code enabled its customization for our specific problem setup. In particular, the RANS solver was first extended to include a dual-time-stepping algorithm for time integration which allows the control of the physical time step. Then, it was adapted for the modeling of the expansion tube. In this section the extensions implemented in the RANS solver will be described.

3.1. Dual-time-stepping method

For solving the unsteady problem, the code was equipped with the dual-time-stepping method introduced by Jameson (1991). A BDF2 (second-order backward difference) scheme was extended by a pseudo-time iteration scheme to solve for a steady state within each physical timestep Δt . The set of equations for the original BDF2 scheme reads

$$\frac{3}{2\Delta t}\mathbf{w}^{n+1} - \frac{2}{\Delta t}\mathbf{w}^n + \frac{1}{2\Delta t}\mathbf{w}^{n-1} + \frac{1}{V}\mathbf{R}(\mathbf{w}^{n+1}) = 0, \quad (3.1)$$

where \mathbf{w} denotes the vector of conserved variables, $\mathbf{R}(\mathbf{w})$ the residual, and V the cell volume. When adding a time derivative in pseudo-time t^* , a modified set of equations

$$\frac{\partial \mathbf{w}}{\partial t^*} + \frac{3}{2\Delta t}\mathbf{w} + \frac{1}{V}\left[\mathbf{R}(\mathbf{w}) - \frac{2V}{\Delta t}\mathbf{w}^n + \frac{V}{2\Delta t}\mathbf{w}^{n-1}\right] = 0 \quad (3.2)$$

is obtained. The solution of Equation 3.2 may then be regarded as marching a timestep Δt in physical time and solving a quasi-steady-state problem within each physical timestep as a fix-point-iteration. Several schemes were implemented, such as an explicit and implicit formulation, as well as three- and four-step Runge-Kutta schemes.

Extensive testing of the numerical scheme was performed on verification cases, such as the shock tube problem by Sod (1978) (see Figure 3). During verification, a numerical instability, known as the Carbuncle phenomenon reported by Peery & Imlay (1988), was

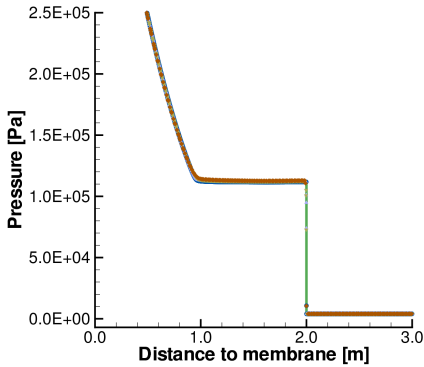


FIGURE 5. Axial grid study performed under similar initial conditions as the final three-dimensional simulation. Tested mesh densities were 1200, 2400, 4800, 9600 and 19,200 cells/meter (shown as Diamond, Gradient, Delta, Circle symbols and solid line, respectively).

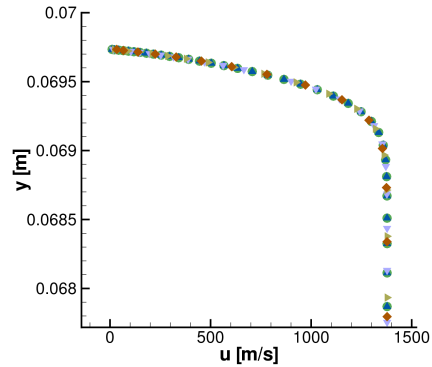


FIGURE 6. Radial grid independence study: velocity profile of the developed boundary layer in a channel flow with inlet boundary conditions similar to the post-shock conditions. Tested mesh densities were 25, 30, 40, 60 and 120 radial cells (Diamond, Triangle, Gradient, Delta and Circle symbols).

observed. This phenomenon creates an instability at the shock front for high Mach number inviscid flows and it is observed when an HLLC approximate Riemann solver is used on two-dimensional cartesian grids. An example of the observed characteristic pattern is presented in Figure 4. However, we have observed that viscous damping eliminates this phenomenon in areas where boundary layer effects predominate.

3.2. Expansion tube modeling

Because the RANS solver cannot treat axisymmetric flows, the expansion tube was modeled as a narrow three-dimensional slice of the full-scale geometry assuming circumferential periodicity. In this fashion, axisymmetry was effectively enforced.

Extensive grid studies have been conducted to identify the requirements for the spatial discretization. Figures 5 and 6 summarize the results of these verification studies. A dimensionless wall coordinate $y^+ < 1$ has been ensured for the flow conditions under investigation. Similar studies have been conducted to determine the timestep sizes of the physical and pseudo-time iterations. As a result of the verification studies, the expansion tube was discretized with 40 cells in the radial direction and 1000 cells/meter in the axial direction for a total of about 478,400 grid cells.

For the results presented in this study, we have selected a forward Euler inner iteration scheme for solving Equation 3.2 in pseudo-time in consideration of the computational costs. We use a second-order MUSCL scheme with TVD limiter for the spatial discretization (van Leer 1979). The convective fluxes are reconstructed by the HLLC approximate Riemann solver of Toro *et al.* (1994). To account for turbulent dissipation and transport, the turbulence model by Spalart & Allmaras (1994) was used. The different gas properties were included by introducing a mixture fraction Z_m which is transported by convection only ($Z_m = 1$ for air, $Z_m = 0$ for helium). Temperature-dependent thermodynamic properties of the test gas (air) were modeled using the NASA polynomials. Flow disturbances or energy losses associated with the interaction of the gas flow with diaphragms and their rupturing process were not included in the current model. Finally,

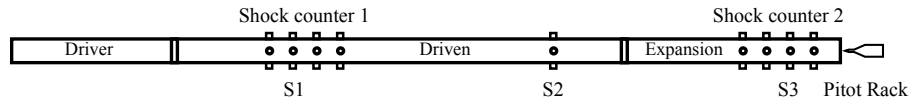


FIGURE 7. Experimental setup and sensor positions

the round/square/round transition of the tube cross-section at the diaphragm stations was not included in the numerical model.

4. Experimental setup

A single condition of operation nominally identical to the condition used in the recent supersonic combustion experiments of Gamba *et al.* (2011) in this facility was considered. The expansion tube was instrumented for the measurement of shock speed, wall-static and stagnation pressure time histories in order to investigate the dynamic process of the system of shock/expansion waves, the viscous-induced shock attenuation, the impact of boundary layer growth on test gas properties, uniformity and test time. Furthermore, in an attempt to further characterize the boundary layer developing along the tube wall heat flux time history measurements were attempted. However, this last effort is subject of ongoing work and it will not be presented in this study. Finally, the direct measurements of test gas temperature and velocity of Strand & Hanson (2011*b*) are used to quantify further the test gas properties.

4.1. Pressure measurements

A schematic diagram of the instrumentation setup is presented in Figure 7. Shock speed was measured at two shock counter stations each located at the driven and expansion sections. Each station was composed of four consecutive pressure transducers 30.5 cm apart. Shock speeds reported further below were computed based on the average time-of-flight between the four transducers. Wall pressure was measured at three locations using Kistler 603B1 dynamic pressure transducers. The three sensors were positioned at $x_{S1} = 2.65$ m and $x_{S2} = 5.54$ m from the primary diaphragm in the driven section, and at $x_{S3} = 8.88$ m in the expansion section. A new rack for pitot pressure probes was designed and manufactured to acquire time-history profiles of the stagnation pressure at several radial locations at the tube outlet. The pitot probes were instrumented with PCB Piezotronics 111A26 and 113A26 dynamic pressure transducers.

4.2. Wavelength-modulation absorption spectroscopy experiments

Figure 8 provides a plan-view illustration of the tunable diode laser absorption spectroscopy (TDLAS) diagnostic applied within the test section of the Stanford Expansion Tube Facility. The diagnostic was recently used in our facility to provide quantitative time histories of the temperature, velocity, and H_2O mole fraction of the test gas (Strand & Hanson 2011*b*). The diagnostic employs two NEL fiber-coupled distributed feedback lasers each tuned to a specific H_2O rovibrational transition. Both lasers are multiplexed onto the same fiber and pitched across the test flow as three beams, one oriented perpendicularly to the flow at 88.25 mm from the end of the expansion section and the other two angled at 45° upstream and downstream relative to the direction of flow, with a centerline crossing location of 215.75 mm from the end of the expansion section. To ensure that only the core flow of the facility is probed, the diagnostic is realized in conjunction

with a parallel-plate flow cutter of 15 mm by 75 mm inlet cross-section aligned with the longitudinal axis of the tube at 15.75 mm from the end of the expansion section.

The perpendicular beam provides line-of-sight averaged temperature and H₂O mole fraction measurements at the furthest possible upstream location to minimize the impact of boundary layer growth within the flow cutter. The pair of angled beams, in combination, provide a measurement of flow velocity and, independently, each of them also provides a measurement of temperature and H₂O mole fraction. The measurements from the angled beams represent a line-of-sight average over the region spanning 178.25 mm to 253.25 mm from the expansion section exit. All beams are positioned 7 mm above the lower wall of the flow cutter.

The laser tuning technique scanned wavelength-modulation absorption spectroscopy (scanned-WMS) developed by Strand & Hanson (2011*a*) is implemented in the diagnostic to enable the simultaneous measurement of temperature, velocity, and H₂O mole fraction at a temporal resolution of 40 μ s. This technique provides high measurement accuracy ($\pm 2\%$) and precision ($\pm 2\%$), as verified in heated optical cell measurements.

5. Results

In this section the results of the numerical simulations will be presented. First, the results will be validated with the available measurements conducted as part of this study and with the measurements of Strand & Hanson (2011*b*). Then, the impact of viscous effects on the dynamics of the process will be discussed. To conclude this section, the final properties of the test gas found at the test section will be presented.

In order to isolate the processes associated with the rupture of the secondary diaphragm from the ones associated with the propagation of the primary shock, computations and experiments were conducted in what we refer to as *shock* and *expansion* modes. In the former mode the facility was operated without the secondary diaphragm, effectively similar to a shock tube without a reflecting end wall; in the latter mode the facility was operated as a traditional expansion tube. When operated in shock mode, the section housing the secondary diaphragm was replaced with a round, constant cross-section segment; this modification eliminates any influence that the change in cross-section might have on the shock propagation process. For each mode of operation, twelve repetitions of the experiments were carried out and, unless stated otherwise, are presented in the following sections as an ensemble average (with corresponding standard deviation indicated as the error bar).

5.1. Shock attenuation due to viscous effects

Figure 9 shows the predicted primary shock Mach number (lines) compared to measured values (symbols) as a function of position along the tube for operation in both shock and expansion mode. Results of the viscous (solid line) and inviscid (dashed line) simulations are presented. Measurements for each independent run are marked separately.

Consider first the results of the shock mode study. When operated in this mode, the shock counters at the two stations effectively measure the primary shock at two downstream locations from which shock attenuation can be inferred. Shock Mach number measurements at the first shock counter station reveal a mild shot-to-shot variability, about 0.3% of the mean value. Conversely, the shock Mach number measured further downstream shows virtually no variability ($< 0.1\%$). The variability observed at the first station might be due to the rupturing process of the primary diaphragm. However, memory of this imperfection appears to be attenuated, if not completely eliminated, as the

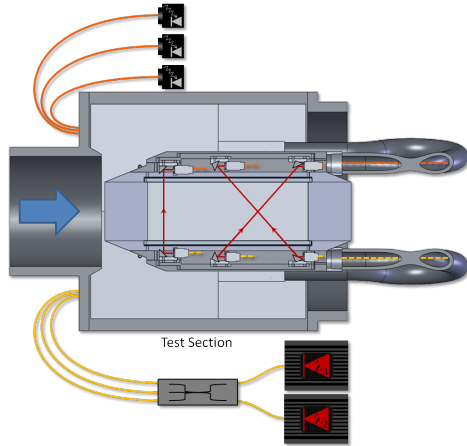


FIGURE 8. Plan view schematic of the Stanford Expansion Tube Facility test section with parallel-plate flow cutter and TDLAS diagnostic installed.

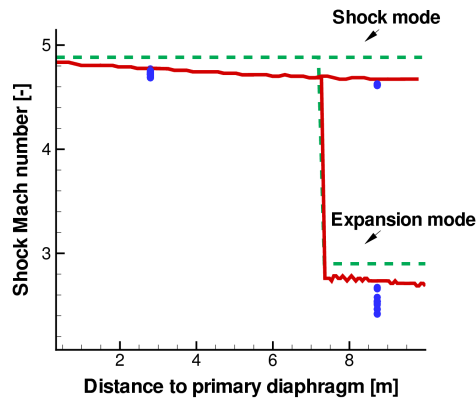


FIGURE 9. Shock Mach number for inviscid simulation (dashed line), viscous simulation (solid line) and individual experiments (symbols) for shock and expansion tube mode.

shock evolves further downstream. The high repeatability in the primary shock Mach number best exemplifies the high repeatability of this facility. Measurements at the two stations also reveal an attenuation of shock Mach number of about 2.5% over the distance separating the two shock counter stations; this results in a spatial attenuation of about 0.4%/meter. Inviscid calculations, as the dash line indicates in Figure 9, would predict a constant shock Mach number along the whole tube. Conversely, the viscous calculation (solid line) predicts the correct trend and relative attenuation, although the simulation predicts a value that is about 1.0% higher than the measured value. The discrepancy between measured and predicted value is believed to be a result of omitting the effects of the primary diaphragm in the model.

When operated in expansion mode, the second shock counter station is used to infer the secondary shock Mach number. In this mode of operation, two observations can be made from the results of Figure 9: (1) the shot-to-shot variability greatly increases ($\sim 3\%$ of the mean value); (2) the measured value is significantly lower than the inviscid ($\sim 12\%$) and viscous ($\sim 7\%$) solutions. It is believed that the increase in the variability of the secondary shock Mach number is the result of an inconsistent and non-ideal rupture process of the secondary diaphragm. Similarly, a lower than expected secondary shock Mach number can be attributed to inertial effects associated with rupture and acceleration of the secondary diaphragm and to partial reflection of the incident primary shock (Furukawa *et al.* 2007).

5.2. Effects of boundary layer growth on post-shock flow properties

The results of Figure 9 indicate the effects of boundary layer formation and growth on shock wave attenuation. Wall static pressure measurements are now used to refine the understanding of these effects on post-shock properties. Figure 10 shows time histories of wall pressure extracted simultaneously at three locations along the tube (details on the locations can be found in a previous section). Measurements (solid line) and inviscid (dashed line) and viscous (dash-dotted line) calculations are also shown.

Consider first the pressure trace at the first location (e.g., in shock mode) shown in Figure 10. Without considering at this stage any oscillation in the traces, measurements show that, upon arrival of the primary shock, the static pressure rises instantaneously

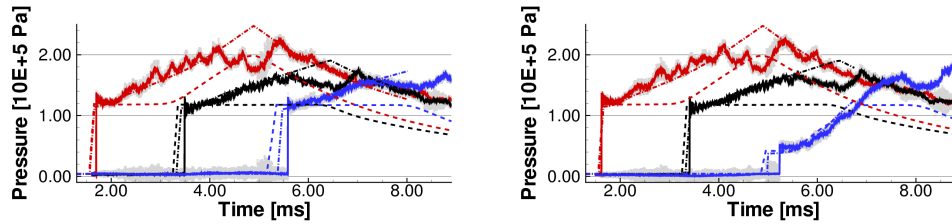


FIGURE 10. Static wall pressure in shock mode (left) and expansion mode (right): inviscid simulation (dashed line), viscous simulation (dashed-dotted line) and experiment (solid line). Sensors positioned at $x_{S1} = 2.65$ m, $x_{S2} = 5.54$ m and $x_{S3} = 8.88$ m from the primary diaphragm (from left to right). Time $t = 0$ s corresponds to the rupturing of the primary diaphragm.

to the post-shock value, stays constant for a small time period, and then begins rising gradually (at about 2 ms). By contrast, the inviscid solution predicts a departure from the constant, post-shock value much later in time (at about 3.2 ms). The pressure increase in the inviscid solution is associated with the arrival of the expansion wave tail and peaks at a time (about 5 ms) which is associated with the arrival of the reflected expansion wave front. As a result, after this time, the pressure drops. The early departure from a constant pressure value observed in the experiment appears to be due to boundary layer growth after the incident shock passage. The displacement effect of the growing boundary layer acts to decelerate and hence compress the incoming flow. Similar effects are observed at the other two measurement locations (in shock mode). The viscous simulation captures the behavior observed in the measurements well. The agreement with measurements extends to all three three locations (in shock mode), although a time lag exists between predicted and measured quantities as the shock speed is overpredicted.

Consider now the results in expansion mode. In particular, consider the pressure time history at the third location. For this case there is a larger discrepancy between measurement and viscous calculations, which gives reason for further investigations. However, the qualitative behavior is fairly well captured by the viscous simulation. Note, however, that in this particular case the gradual rise in pressure is predominantly due to the arrival of the secondary expansion wave as viscous and inviscid calculations are in good agreement.

We point out that the measurements presented in Figure 10 are an average of 12 runs (with standard deviation shown in the gray band) and the excellent repeatability of these pressure traces, along with any of their features. For example, the low-frequency oscillations that are observed in the trace at the first location are very repeatable and are believed to be due to disturbances introduced by the rupturing and interference effect of the primary diaphragm. On the other hand, these flow disturbances appear to attenuate further downstream. Similarly, some of the low-frequency oscillations observed in the time trace in expansion mode at location 3 could be induced by flow distortion due to the second diaphragm and by the change in cross-section at the diaphragm station.

5.3. Spatial and temporal characteristics of the outflow

After considering the processes occurring along the tube, we now focus on the assessment of the outflow characteristics at the test section. We will first consider pitot pressure measurements on the exit plane as a last validation step. Figure 11 shows time histories of the measured and simulated pitot pressure at two selected positions: within the boundary layer (6.5 mm away from the wall) and in the core flow (23.1 mm from the tube centerline).

After the secondary shock arrival, the stagnation pressure in the helium expansion gas

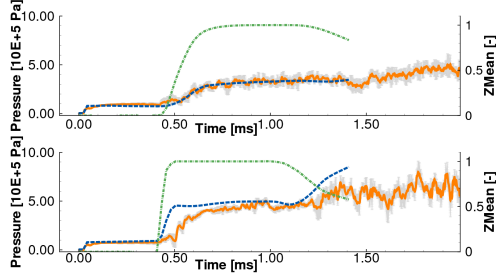


FIGURE 11. Pitot pressure at the test section after shock arrival for experiment (solid line) and simulation (dashed line) 6.5 mm away from the wall (upper figure) and 23.1 mm from the tube centerline (lower figure). Test gas flow is visualized by the mixture fraction (dashed–dotted line).

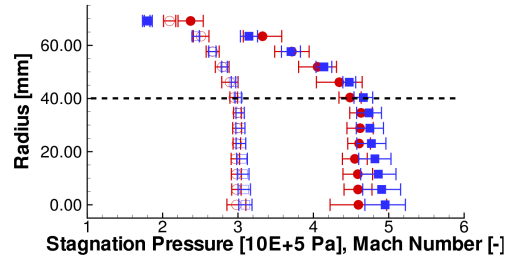


FIGURE 12. Test time-averaged stagnation pressure (filled symbols) and flow Mach number (open symbols) from numerical simulation (square) and experiments (round). Error bars indicate one standard deviation about the test time average.

flow rises to approximately 100 kPa. A second rise in stagnation pressure indicates the arrival of the test gas (air) in its final state and hence marks the beginning of the test gas flow. The test gas flow is ended by the arrival of the primary contact surface, which causes another pressure rise approximately 1.2 ms after the initial shock arrival. In the viscous boundary layer, there is excellent agreement between experiment and simulation. Conversely, in the core flow the pitot pressure is overpredicted by approximately 4%, which could result from the overprediction of the shock Mach numbers. Furthermore, the prediction indicates a faster pressure rise at the arrival of the expansion/test gas contact surface than what was observed in the experiment. However, the slow rise observed in the experiment could be an artifact resulting from limitations in pitot probe response characteristics (Sutcliffe & Morgan 2001). Finally, from the measurements, the duration of constant pitot pressure (here defined as test time) is estimated to be approximately 730 μs , whereas the simulation predicts a shorter duration of approximately 650 μs .

Pitot pressure measurements are also used to quantify the radial extent of uniform flow. Figure 12 shows average pitot pressure and inferred flow Mach number across the tube radius. Values presented in the figure were averaged over the test time; the error bars refer to the standard deviation. In the experiment, the flow Mach number was estimated assuming a nominal static pressure of 40 kPa and a ratio of specific heats of 1.33. Although the quantitative comparison between measurements and prediction is only fair, the viscous simulation well captures the size of the inviscid core. As a result, a region of approximately 40 mm in radius from the tube centerline (indicated by the dashed line) of uniform flow is identified. Note that the viscous simulation shows a higher pitot pressure near the tube centerline where limited convergence due to non-optimal grid-size aspect ratio was experienced, and could be another cause for the observed disagreement with measurements near the tube centerline.

5.4. Quantification of test gas properties

The previous steps served as validation of the computation but also provided some insight into the impact of boundary layer growth. In general, we found good agreement between measurements and computations, although discrepancies in shock speeds, which affect post-shock conditions, were observed. In spite of the differences, in this section we will attempt to estimate the test gas properties at the tube outlet and we will compare them with the direct measurements of Strand & Hanson (2011b).

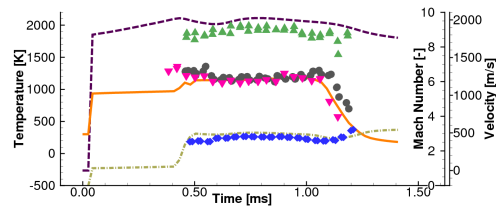


FIGURE 13. Numerical (lines) and TDLAS measurements (symbols) of velocity, temperature and Mach number (from top to bottom).

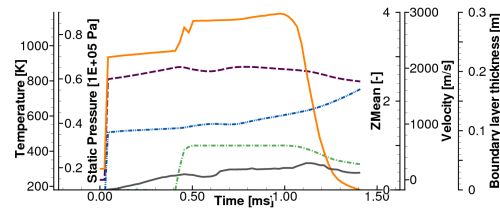


FIGURE 14. Gas properties in the core flow from RANS simulation: temperature, velocity, static pressure, mixture fraction and 99%-boundary layer thickness (from top to bottom).

Figure 13 shows a comparison of measured time histories of flow temperature, velocity and Mach number (Strand & Hanson 2011b) with the results of the viscous simulation. Focusing on the temperature history, temperature first jumps at the arrival of the secondary shock (expansion gas flow), it experiences a weak increase during the expansion gas flow and then rises to the test gas value at the arrival of the expansion/test gas contact surface (at 0.5 ms). During the test time, temperature shows a weak increase at first, but then rises more rapidly in the second portion of the test time until the driver/test gas contact surface arrives. Measurements, which are available only in the test gas, show a very similar profile and compare well with the computed values. The main difference is at the beginning of the test time where temperature rises above the predicted value and then falls back onto the predicted curve. However, the overshoot in measured temperature at early times might be due to interference effects of the measurement instrumentation. Note, however, that the TDLAS measurements were performed in air seeded with 8% water, in which case temperature is expected to be about 3% lower than for dry air.

The velocity history, in contrast, shows a larger discrepancy with measurements: over-prediction of about 7%. A similar result holds for the Mach number. This result is consistent with the fact that predicted shock speeds are higher than observed, and thus higher temperature and velocities are expected. The difference in the velocity profiles agrees with this intuitive argument, but temperature prediction contradicts this reasoning.

The temporal variations of test gas properties are further presented in Figure 14. In this figure, the mixture fraction Z_m is shown to identify the test gas flow. The 99% boundary layer thickness over time is extracted from the velocity profile approaching the outlet. The window of constant stagnation pressure starts at approximately 470 μ s after the shock arrival. It ends at approximately 1,120 μ s and thus spans over a range of approximately 650 μ s. The static pressure, other the other hand, remains constant only for approximately 250 μ s after the arrival of the test gas and then gradual rises to about 20% of the initial value by the end of the test time. Consider now the boundary layer thickness. With the arrival of the expansion gas, the viscous boundary layer starts forming, which is believed to cause a rise in static pressure and speed. The thickness of the boundary layer reaches a peak value at the time of arrival of the primary contact surface. Between 470 μ s and 720 μ s, which corresponds to the transition from expansion to test gas flow over the whole cross section of the outlet plane, the boundary layer thickness shows first a drop and then a rise. At this stage the temperature remains nearly constant, whereas the velocity shows a dip and pressure a rise. During the test gas flow, the boundary layer thickness begins to increase linearly, which induces a corresponding linear increase in static pressure and a decrease in flow velocity.

Model	Temperature [K]	Velocity [m/s]	Static Pressure [kPa]	Mach number
RANS Simulation	1153 ± 22	1989 ± 26	40.9 ± 1.8	2.99 ± 0.06
TDLAS	1155 ± 42	1846 ± 51	~ 40	2.72 ± 0.10
Ideal	1250	1934	40	2.8

TABLE 1. Summary of the test time-averaged test gas conditions from simulation, TDLAS measurements (Strand & Hanson 2011*b*) and zero-dimensional ideal analysis (Gamba *et al.* 2011). The variability over the mean refers to the standard deviation over the test time.

6. Conclusions

A quantitative estimate of the test gas conditions is obtained from an average over the steady portion of test gas flow. The numerical values are presented in Table 1 with direct measurements and the original estimates from the ideal flow solution. The current viscous simulations show a significantly lower temperature than original estimates but are close to the measured value. By contrast, the estimated Mach number is about 7 – 10% higher than what was originally estimated and measured. Some of these differences could be due to the higher prediction of shock Mach number and to diaphragm effects. The lower predicted temperature also results from considering variable thermodynamic properties, unlike the original estimate.

In general, the viscous simulations are capable of capturing crucial characteristics of the unsteady flow development and the impact of boundary layer growth on observable quantities. The overestimation of the shock Mach numbers in the simulation may explain some discrepancies between the computational and experimental results. Boundary layer formation is found to have a major impact on the test gas flow, causing a steady rise in static pressure and hence inhibiting a test gas flow at fully steady conditions.

Acknowledgments

This work was supported by the US Department of Energy under the Predictive Science Academic Alliance Program (PSAAP). The authors gratefully acknowledge the help of Dr. Francisco Palacios during the code developing phase. F.Ö. wishes to acknowledge the support of the Max-Weber-Programm der Studienstiftung des Deutschen Volkes (MWP) and the support of the Institute of Aerodynamics and Fluid Mechanics at Technische Universität München. C.S. wishes to acknowledge the support of the National Sciences and Engineering Council of Canada (NSERC).

REFERENCES

- FURUKAWA, T., AOCHI, T. & SASOH, A. 2007 Expansion tube operation with thin secondary diaphragm. *AIAA J.* **45** (1), 214–217.
- GAMBA, M., MILLER, V. A., MUNGAL, M. G. & HANSON, R. K. 2011 Ignition and flame structure in a compact inlet/scramjet combustor model. In *17th AIAA International Space Planes and Hypersonic Systems and Technologies Conference, Paper AIAA-2011-2366*.
- HELTSLEY, W. N., SNYDER, J. A., HOULE, A. J., DAVIDSON, D. F., MUNGAL, M. G. & HANSON, R. K. 2006 Design and characterization of the standard 6 inch expansion tube. *AIAA Aerospace Sciences Meeting, Paper AIAA-2006-4443*.

- JAMESON, A. 1991 Time dependent calculations using multigrid, with applications to unsteady flows past airfoils and wings. In *AIAA 10th Computational Fluid Dynamics Conference*.
- VAN LEER, B. 1979 Towards the ultimate conservative difference scheme, v. a second order sequel to Godunov's methods. *J. Comput. Phys.* **32**.
- MIRELS, H. 1963 Shock tube test time limitation due to turbulent-wall boundary layer. *AIAA J.* **2**(1), 84–93.
- MIRELS, H. 1966a Correlation formulas for laminar shock tube boundary layer. *Phys. Fluids* **9**(7), 1265–1272.
- MIRELS, H. 1966b Flow nonuniformity in shock tubes operating at maximum test times. *Phys. Fluids* **9**(10), 1907 – 1912.
- PAULL, A. & STALKER, R. J. 1992 Test flow disturbances in an expansion tube. *J. Fluid Mech.* **245**, 493–521.
- PECNIK, R., TERRAPON, V., HAM, F. & IACCARINO, G. 2009 Full system scramjet simulation. *Center for Turbulence Research Annu. Res. Briefs* pp. 33–56.
- PEERY, K. M. & IMLAY, S. T. 1988 Blunt-body flow simulations. *AIAA Paper* 88-2904.
- ROTHKOPF, E. M. & LOW, W. 1974 Diaphragm opening process in shock tubes. *Phys. Fluids* **17**(6), 1169 – 1173.
- SOD, G. A. 1978 Survey of several finite difference methods for systems of nonlinear hyperbolic conservation laws. *J. Comput. Phys.* **26** (4), 1–31.
- SPALART, P. R. & ALLMARAS, S. R. 1994 A one-equation turbulence model for aerodynamic flows. *La Recherche Aérospatiale* **1** (1), 5–21.
- STRAND, C. L. & HANSON, R. K. 2011a Scanned wavelength-modulation absorption spectroscopy. In preparation, 2011.
- STRAND, C. L. & HANSON, R. K. 2011b Thermometry and velocimetry in supersonic flows via scanned wavelength-modulation absorption spectroscopy. In *47th AIAA/ASME/SAE/ASEE Joint Propulsion Meeting and Exhibit - San Diego, CA. Paper AIAA-2011-5600*.
- SUTCLIFFE, M. A. & MORGAN, R. G. 2001 The measurement of pitot pressure in high enthalpy expansion tubes. *Measurement Science and Technology* **12**, 327–334.
- TERRAPON, V. E., PECNIK, R., HAM, F. & PITSCH, H. 2010 Full-system rans of the hyshot II scramjet part 2: Reactive cases. *Center for Turbulence Research Annu. Res. Briefs* pp. 69–80.
- TORO, E., SPRUCE, M. & SPEARES, W. 1994 Restoration of the contact surface in the HLL-Riemann solver. *Shock Waves* **4**, 25–34.
- TRIMPI, R. L. 1962 A preliminary theoretical study of the expansion tube, a new device for producing high-enthalpy short-duration hypersonic gas flows. *Tech. Rep.*. National Aeronautics and Space Administration.
- WALKER, J. & DENNIS, S. 1972 The boundary layer in a shock tube. *J. Fluid Mech.* **56**, 19–47.
- WHITE, D. R. 1958 Influence of diaphragm opening time on shock-tube flows. *J. Fluid Mech.* **4**, 585.